applied mechanics

Article

Free Vibration of Agglomerated SiO_2 Nanoparticle-Reinforced Concrete Beams on Elastic Foundations

Hichem Rakib Sebbagh [1], Zouaoui R. Harrat [2,*], Mohammad I. Al Biajawi [3], Mohammed Chatbi [4] and Ehsan Harirchian [5]

[1] Civil Engineering Department, Laboratoire de Mécanique, des structures, et stabilité des Constructions (LM2SC), University of Science and Technology of Oran Mohamed Boudiaf (USTO-MB), B.P. 1505 El M'naouer, Oran 31000, Algeria
[2] Laboratoire des Structures et Matériaux Avancés dans le Génie Civil et Travaux Publics, Djillali Liabes University, Sidi Bel-Abbes 22000, Algeria
[3] Shenzhen International Graduate School, Tsinghua University, Shenzhen 518055, China
[4] Department of Public Works, University Mouloud Mammeri, Tizi Ouzou 15000, Algeria
[5] Institute of Structural Mechanics (ISM), Bauhaus-Universität Weimar, 99423 Weimar, Germany
* Correspondence: zouaoui.harrat@univ-sba.dz

Abstract

Nano-silica can stiffen cementitious composites, but its benefit depends on how well the nanoparticles are dispersed, and agglomeration is common in the alkaline pore solution of cement paste. This study presents an analytical framework for the free vibration of SiO_2 nanoparticle-reinforced concrete beams resting on a Winkler–Pasternak elastic foundation, with nanoparticle agglomeration explicitly incorporated into the effective properties. Agglomeration is described by two parameters: the volume fraction of nanoparticle-rich inclusions, ξ, and the fraction of nanoparticles located within them, ζ. These parameters enter a two-stage homogenization scheme that combines a Voigt–Reuss estimate for each region with Paul's model for the composite, and their admissible range is derived from the volume-fraction constraints. The resulting properties are embedded in a three-unknown higher-order shear deformation theory that satisfies the traction-free surface conditions without a shear correction factor. The governing equations are derived from Hamilton's principle and solved analytically for simply supported, clamped–clamped and clamped–simply supported beams. The beam formulation agrees with published benchmarks for functionally graded beams to within 0.03% without a foundation and 0.6% on a Winkler–Pasternak foundation. For a fixed matrix and hydration state, increasing the SiO_2 volume fraction from 0 to 0.20 raises the fundamental frequency by about 14% for all three boundary conditions. This gain comes almost entirely from stiffening, since the change in density contributes less than 1%. When half of the nano-silica is agglomerated and does not contribute to load transfer, this gain falls to about 8%, so roughly half of the dynamic benefit is lost. Over the investigated range of dimensionless foundation stiffness, the Pasternak parameter raises the frequency more than the Winkler parameter, and clamped–clamped beams give the highest frequencies, followed by clamped–simply supported and simply supported beams. The framework links dispersion quality, boundary restraint and foundation support to the dynamic response of nano-engineered concrete members.

Keywords: agglomeration effect; free vibration; higher-order shear deformation theory; nanoparticle-reinforced concrete beam; SiO_2 nanoparticles; Winkler–Pasternak foundation

Received: 22 September 2026
Revised: 29 October 2026
Accepted: 3 November 2026
Published: 4 November 2026

Copyright: © 2026 by the authors. Licensee MDPI, Basel, Switzerland. This article is an open access article distributed under the terms and conditions of the Creative Commons Attribution (CC BY) license.

1. Introduction

Concrete remains the most widely consumed construction material worldwide, and civil infrastructure elements such as beams, slabs, and foundations are routinely designed for service lives exceeding a century [1]. Despite its ubiquity, conventional Portland-cement concrete suffers from intrinsic brittleness, a relatively low tensile-to-compressive strength ratio, and a porous microstructure that limits its durability under aggressive environmental and dynamic loading conditions [2,3]. Over the past two decades, nanotechnology has opened a new frontier for tailoring the microstructure of cementitious composites. Accordingly, nanoparticles such as nano-silica (SiO_2), nano-titania (TiO_2), nano-alumina, nano-$CaCO_3$, carbon nanotubes (CNTs), and graphene-based fillers have been extensively investigated as reinforcing or pozzolanic additives for concrete [4–8]. Among these materials, SiO_2 nanoparticles have attracted particular attention because of their high specific surface area and pronounced pozzolanic reactivity. Upon reacting with the calcium hydroxide liberated during cement hydration, nano-SiO_2 promotes the formation of additional calcium-silicate-hydrate (C-S-H) gel, densifies the interfacial transition zone, refines the pore structure, and consequently enhances compressive, flexural, and tensile strength as well as long-term durability [9]. Recent studies have further shown that the mechanical benefits of silica-based additives can be enhanced through hybridization with graphene-based nanomaterials. Chen et al. [10] investigated high-volume supplementary cementitious material systems containing ground granulated blast-furnace slag and fly ash, and reported that the combined addition of 0.05 wt% graphene oxide and 5 wt% silica fume refined the pore structure and promoted the formation of a hybrid nanostructure involving low- and high-polymerized C-S-H. This synergistic interaction increased the 28-day compressive and flexural strengths by 20.11% and 15.10%, respectively, relative to the control mixture. Such findings underline that the mechanical efficiency of nano- and micro-silica additions is governed not only by their dosage but also by their dispersion state, reaction products, and interaction with the cementitious matrix.

Despite these advantages, a recurring complication in nano-modified cementitious systems is the tendency of nanoparticles to agglomerate rather than disperse uniformly throughout the cement matrix. In the highly alkaline, calcium-rich pore solution of fresh cement paste, electrostatic double-layer repulsion between SiO_2 nanoparticles is suppressed by high ionic strength and multivalent cation bridging, causing the particles to cluster into micron-scale agglomerates [11,12]. Numerous experimental studies employing zeta-potential measurements, dynamic light scattering, and electron microscopy have confirmed that such agglomeration alters the effective particle size distribution, modifies pore-structure refinement, and can locally offset the mechanical benefits nominally expected from the nanoparticle content [13,14]. Because agglomerated clusters behave mechanically as larger, more compliant inclusions rather than as isolated stiff nanoparticles, the effective elastic properties of the nanoparticle-reinforced matrix may deviate substantially from predictions based on simple rule-of-mixtures or dilute-inclusion models [15]. This behavior highlights the need for micromechanical homogenization schemes capable of explicitly accounting for nanoparticle agglomeration.

In this context, predicting the effective elastic properties of a composite from its constituent phases has long relied on micromechanics-based homogenization schemes of increasing sophistication. Early efforts by Voigt [16] and Reuss [17] established simple parallel and series mixing rules that provide upper and lower bounds on the effective elastic moduli of a composite, although these bounds can be quite wide and physically unrealistic for many reinforcement geometries. Hashin and Shtrikman [18] later derived tighter

https://doi.org/10.3390/applmech7040091

variational bounds for the elastic moduli of composite materials, improving upon the simplicity of the rule-of-mixtures approach. A major advance came with Eshelby's solution [19] for the elastic field of an ellipsoidal inclusion embedded in an infinite matrix, which laid the theoretical foundation for essentially all subsequent mean-field homogenization schemes. Building on this framework, Mori and Tanaka [20] proposed a micromechanical model that relates the average stress and strain in the reinforcement to those in the matrix using an Eshelby-type equivalent inclusion approach. This Mori-Tanaka scheme was later reformulated by Benveniste [21] into a more compact and widely used tensorial form. Because the Mori-Tanaka model assumes a dilute distribution of inclusions in an infinite matrix, it captures the effective properties of composites reasonably well at low filler volume fractions but does not explicitly account for particle-particle interactions or clustering. This limitation is particularly relevant to nanoparticle-reinforced systems, in which nanoparticles tend to agglomerate into clusters rather than disperse uniformly within the matrix. Consequently, several researchers have extended the Mori-Tanaka scheme to explicitly incorporate agglomeration effects when predicting the equivalent properties of nanocomposites [22–26].

The development of suitable homogenization approaches is closely linked to the need for accurate structural theories capable of describing the response of nanoparticle-reinforced members. Beam theory has evolved considerably to balance simplicity with accuracy in predicting structural response. The classical Euler-Bernoulli theory, formulated in the mid-18th century, remains foundational for slender beams but neglects transverse shear deformation, limiting its accuracy for thick or short members. To address this limitation, Timoshenko [27] developed a first-order shear deformation theory in the early 20th century that accounts for shear deformation and rotary inertia, making it more suitable for thick beams and high-frequency vibration problems. However, this first-order approach requires an empirical shear correction factor to compensate for the unrealistic assumption of constant shear strain through the thickness, which motivated the development of higher-order shear deformation theories (HSDT) [28]. Reddy [29] proposed a widely used third-order shear deformation theory that better predicts the response of thick beams without requiring a shear correction factor, while later refinements introduced trigonometric [30], hyperbolic [31], and exponential [32] shear shape functions to further improve the representation of transverse shear stress distribution across the beam thickness.

These HSDT formulations have subsequently been extended to nanocomposite and civil engineering applications. Zamanian et al. [33] studied the effect of nanoparticle agglomeration on the buckling response of embedded concrete columns reinforced with SiO_2 nanoparticles, finding that agglomeration effects reduce the buckling load. Shokravi [34] analyzed the buckling behavior and active control of ZnO nanoparticle-reinforced concrete beams on elastic foundations, using hyperbolic beam theory, the Mori–Tanaka model, and the differential quadrature method to examine the effects of nanoparticle content, voltage, boundary conditions, and beam geometry. In parallel, Jafarian Arani and Kolahchi [35] analyzed the buckling behavior of concrete columns retrofitted with a CNT-reinforced polymer layer using both Euler-Bernoulli and Timoshenko beam models. Building on this trajectory, recent work has applied a higher-order shear deformation theory combined with Eshelby's model to derive equivalent nanocomposite properties and comparatively investigate the buckling and free vibration behavior of concrete beams reinforced with various types of nanoparticles resting on multi-parameter elastic foundations [36]. These studies underscore the growing importance of HSDT-based frameworks for accurately capturing the coupled bending-shear response of nanoparticle-reinforced concrete members.

In addition to the beam formulation and homogenization approach, the mechanical interaction between a structural member and its supporting medium plays an important role in its dynamic response. Modeling this interaction has evolved from simple spring analogies toward increasingly refined multi-parameter continuum representations. The earliest and most widely used model was proposed by Emil Winkler in 1867 [37], representing the foundation as a bed of mutually independent, closely spaced elastic springs whose reaction is proportional to the local deflection. While simple and computationally efficient, the Winkler model's main shortcoming is its inability to capture continuity between adjacent springs, producing unrealistic discontinuities in deflection at loaded/unloaded boundaries. To resolve this limitation, Filonenko-Borodich [38] introduced continuity by connecting the spring elements to a thin elastic membrane under constant tension, while Hetényi [39] achieved a similar coupling effect by embedding an elastic plate or beam capable of bending between the springs. Pasternak [40] later proposed an alternative two-parameter model that introduces shear interaction between the springs through a layer of incompressible vertical elements deforming only in transverse shear. This model remains one of the most popular two-parameter foundation idealizations in structural mechanics. Kerr [41] subsequently generalized these formulations into a three-parameter model consisting of two elastic spring layers interconnected by an elastic shear layer, showing that both the Winkler and Pasternak models can be recovered as special or limiting cases of this more general representation. These classical foundation idealizations have since been widely combined with beam and plate theories for soil-structure interaction, railway track, and pavement problems [42] and, more recently, have been adopted in the analysis of nanocomposite and nanoparticle-reinforced structural members [43].

Against this background, the present study does not propose a new homogenization rule or beam theory. Its contribution is the coupled analysis, for nano-SiO_2 concrete, of three effects that, to the authors' knowledge, have not previously been examined together: the agglomeration state of the nanoparticles, transverse shear deformation, and the support provided by a two-parameter (Winkler–Pasternak) elastic foundation. Agglomeration is described by two parameters, the inclusion volume fraction ξ and the fraction ζ of nanoparticles located inside the inclusions, and enters the effective properties through a two-stage homogenization scheme. A higher-order shear deformation beam theory with three unknowns is employed to capture transverse shear effects without a shear correction factor, and the governing equations are derived via Hamilton's principle and solved analytically for simply supported, clamped–clamped and clamped–simply supported boundary conditions. Because the solution is closed-form, the interaction between the SiO_2 volume fraction, the agglomeration parameters (ξ, ζ), the slenderness ratio L/h, the beam theory (compared with FSDT using shear correction factors), and the Winkler and Pasternak foundation coefficients can be examined systematically in terms of the dimensionless natural frequency. Applying an established formulation to nano-SiO_2 concrete is not a substitution of input data: the moduli and the matrix–filler contrast differ markedly from the polymer and metal matrices in earlier studies, so the agglomeration trends and frequency sensitivities cannot be inferred from them. The study aims to provide design-oriented insight into how nanoscale dispersion quality and foundation support jointly affect the dynamic performance of nano-engineered concrete beams.

https://doi.org/10.3390/applmech7040091

2. Materials and Homogenization

2.1. Nano-SiO_2

Nanosilica can be synthesized through various methods, including the sol–gel process, thermal decomposition, and vapor-phase deposition. Owing to its strong pozzolanic reactivity and pore-filling capability, nanosilica has become a common additive in cementitious mixtures, where it enhances the hardening behavior of concrete. Consisting of ultra-fine spherical particles averaging around 4 nm in diameter with a correspondingly high surface-area-to-volume ratio, nano-SiO_2 exhibits pronounced reactivity in geopolymerization reactions. When incorporated into alkali-activated binders, nanosilica has been shown to accelerate hydration and polymerization processes, leading to improved mechanical and microstructural properties. Its three key effects in these binders can be summarized as: (i) accelerated hydration, (ii) refined microstructure, and (iii) enhanced mechanical performance.

Nanosilica (nano-SiO_2) is the most widely used nanomaterial in alkali-activated binders [44]. Studies have shown that adding 1% nanosilica to a metakaolin-based geopolymer can produce a significant increase in compressive strength (CS), on the order of 52% after 60 days. However, raising the nanosilica content to 3% led to a decrease in CS, attributed to poor dispersion of unreacted nanoparticles within the matrix and the resulting nano-interaction energy [45]. For coal fly ash (FA)/slag-based geopolymer binders, the optimal nanosilica content was found to be around 2%. It has also been observed that nanosilica inclusion causes a slight delay in hydration while promoting additional calcium–alumina–silicate–hydrate gel formation, which in turn reduces the porosity of the alkali-activated geopolymer [46]. Furthermore, nanosilica has been shown to enhance the degree of geopolymerization, yielding a denser geopolymer paste [47]. Figure 1 presents the micromorphology and microhardness of recycled mortar modified with nanosilica at a cement-to-sand ratio of 1:1. Six points were examined on each specimen: points 1–2 on the recycled fine aggregate, points 3–4 within the interfacial transition zone, and points 5–6 in the hardened cement paste. The microhardness followed the order recycled fine aggregate > cement paste > interfacial transition zone, confirming that the interfacial transition zone represents the weakest region of the mortar. Increasing the nanosilica content from 0% to 2% progressively enhanced the microhardness of all regions, with the 2% mixture reaching a maximum value of 1326 HV. At this content, the interfacial transition zone exhibited a dense and regular microstructure, with pores and microcracks effectively filled by hydration products. In contrast, increasing the nanosilica content to 3% promoted particle agglomeration and reduced dispersion, limiting the pore-filling effect and slightly decreasing the microhardness of the interfacial transition zone and cement paste. The corresponding micrographs also revealed pronounced nanosilica accumulation, indicating a lower modification efficiency at excessive nanosilica content.

In practice, nano-silica does not replace the concrete as a whole: it partly replaces the cement binder, fills the pores and reacts pozzolanically with calcium hydroxide to form additional C-S-H gel, which changes the degree of hydration and the structure of the matrix. These mechanisms are not resolved in the present work. The properties of the matrix are those of the concrete at a given mix and curing age, which already include its hydration state, and the nano-silica is represented as an additional elastic phase defined by its volume fraction. These observations show that agglomeration is a measurable, property-degrading phenomenon above an optimum dosage. They provide the physical basis for describing the dispersion state by the parameters ξ and ζ in Section 2.2. The microhardness values themselves are not inputs of the model.

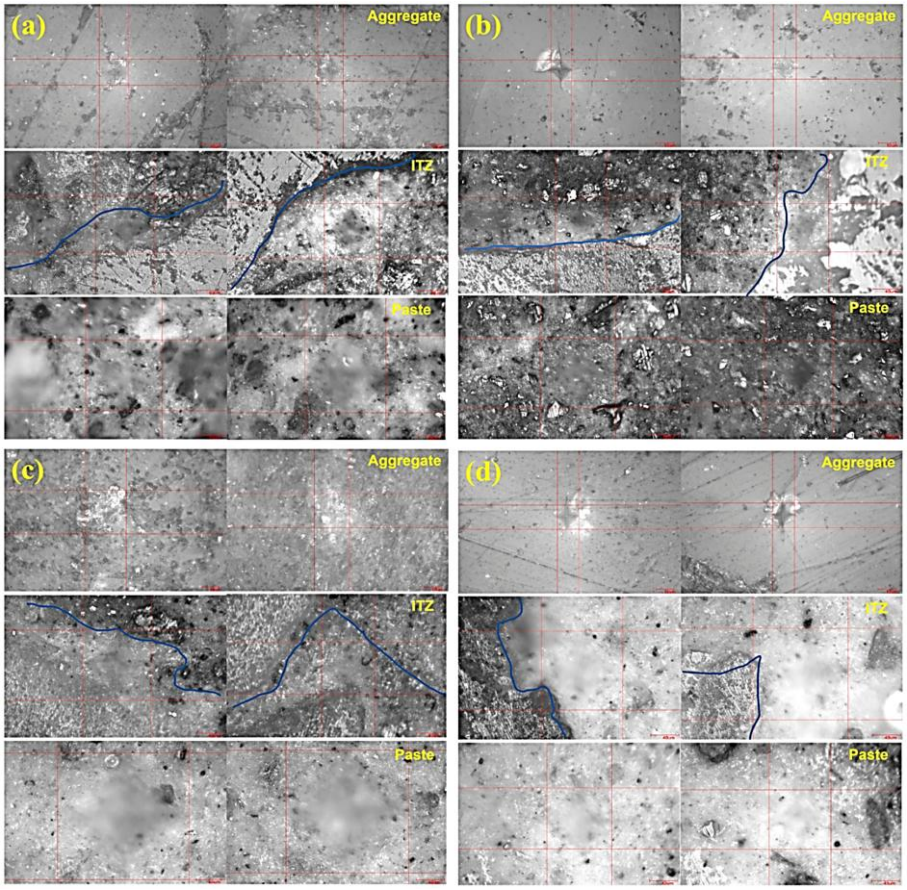


Figure 1. Micromorphology of nano-modified recycled fine aggregate mortar at different NS concentrations: (**a**) 0%; (**b**) 1%; (**c**) 2%; (**d**) 3% [48].

2.2. Two-Stage Homogenization and Agglomeration Effect

In recent years, the use of nano-silica in concrete has garnered increasing attention. Nano-silica is considered to have much finer particle sizes and higher pozzolanic reactivity than silica fume, making it more effective as a filler, pozzolan, and seed material [49,50]. However, nanoparticles in powder form often exist as aggregated (tightly bound clusters) or agglomerated (loosely bound clusters) particles, with final grain sizes ranging from submicron to as large as 100 μm due to their very high specific surface area and energy (see Figure 2). Even in well-dispersed colloidal suspensions, nanoparticles still tend to agglomerate, with grain sizes remaining in the submicron range [51]. It is often assumed that using colloidal silica sol, which contains mono-dispersed nanoparticles, can enhance their effectiveness as fillers and seeds compared to the agglomerates found in powder form or in ordinary dispersions [52,53].

The Voigt model is a micromechanical homogenization approach used to estimate the effective elastic properties of a composite material. It assumes that all phases within the representative volume element (RVE) experience the same strain. Under this iso-strain assumption, the stress carried by each phase is proportional to its elastic modulus and volume fraction. Consequently, the Voigt model generally provides an upper-bound estimate of the effective stiffness of the composite [54].

In the present study, the composite consists of a concrete matrix reinforced with nano-silica particles. The nano-silica particles are assumed to be isotropic. Therefore, any anisotropy associated with their shape or internal structure is neglected. Agglomeration is incorporated by assuming that the nanoparticles are concentrated within spherical regions distributed throughout the concrete matrix. These nanoparticle-rich regions are treated as inclusions with elastic properties different from those of the surrounding

material [55]. The nano-silica is treated as an elastic reinforcing phase, and the chemical reaction with the cement hydration products is not modelled; the results therefore refer to a fixed matrix and hydration state.

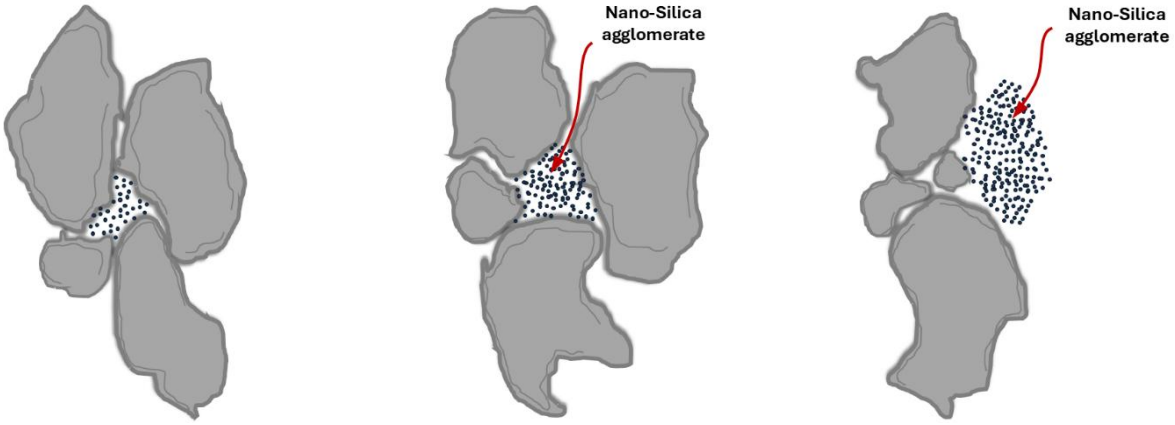


Figure 2. Homogenization procedures of a biphasic material (ordinary concrete + SiO_2 nanoparticles) considering agglomeration effect: (**a**) Sufficient amount of NS; (**b**) Smaller Agglomerates of NS; (**c**) Larger Agglomerates of NS.

Let V denote the total volume of the RVE, $V^{inclusion}$ the total volume occupied by the spherical inclusions, and V^r the total volume of nano-silica particles. The total volume of nano-silica is divided into two contributions:

$$V^r = V_{in}^r + V_{out}^r \tag{1}$$

where V_{in}^r is the volume of nano-silica located inside the spherical inclusions and V_{out}^r is the volume of nano-silica dispersed in the matrix outside the inclusions.

The overall volume fractions of nano-silica and concrete are defined as

$$C_r = \frac{V^r}{V} \tag{2}$$

$$C_m = 1 - C_r \tag{3}$$

where C_r is the total nano-silica volume fraction and C_m is the volume fraction of the concrete matrix.

Two parameters are used to quantify the degree of nanoparticle agglomeration. The first parameter, ξ, represents the volume fraction of the spherical inclusions within the entire composite,

$$\xi = \frac{V^{inclusion}}{V} \tag{4}$$

The second parameter, ζ, represents the fraction of all nano-silica particles that is located inside these inclusions:

$$\zeta = \frac{V_{in}^r}{V^r} \tag{5}$$

Thus, ξ describes the size or spatial proportion of the nanoparticle-rich regions, whereas ζ describes how much of the total nano-silica is concentrated within those regions.

The volume fraction of nano-silica inside an inclusion is obtained by dividing the nano-silica volume inside the inclusion by the following inclusion volume:

$$\phi_{in}^{r} = \frac{V_{in}^{r}}{V^{inclusion}} \tag{6}$$

Similarly, the volume fraction of nano-silica dispersed in the material outside the inclusions is

$$\phi_{out}^{r} = \frac{V_{out}^{r}}{V - V^{inclusion}} \tag{7}$$

For the model to be physically meaningful, both local particle concentrations must satisfy

$$0 \le \phi_{in}^{r} \le 1, \quad 0 \le \phi_{out}^{r} \le 1 \tag{8}$$

These restrictions ensure that the amount of nano-silica assigned to each region does not exceed the volume available in that region.

The limiting values of ξ and ζ have a direct physical interpretation. When $\xi = 1$, the inclusion occupies the entire RVE and no region exists outside it. The mass balance then requires $\zeta = 1$, and the two-region model reduces to a single phase. Uniform dispersion corresponds to $\zeta = \xi$. When $\xi < 1$, the nanoparticles are concentrated in part of the composite whenever $\zeta > \xi$.

When $\zeta = 1$, all nano-silica particles are located inside the spherical inclusions, meaning that no nanoparticles remain dispersed in the surrounding matrix. When $0 < \zeta < 1$, the nano-silica is divided between the inclusion regions and the surrounding matrix. A larger value of ζ, particularly when $\zeta > \xi$, indicates that the nanoparticles are more highly concentrated within the inclusions than they would be under a uniform distribution. Therefore, increasing ζ or decreasing ξ generally represents stronger nanoparticle agglomeration.

The relationship between the agglomeration parameters and the local nano-silica concentrations can be expressed as

$$\phi_{in}^{r} = \frac{\zeta C_r}{\xi} \tag{9}$$

$$\phi_{out}^{r} = \frac{(1-\zeta)C_r}{1-\xi} \tag{10}$$

From Equations (8)–(10), the admissible values satisfy $\zeta Cr \le \xi \le 1 - (1 - \zeta)Cr$. These expressions show that, for a fixed total nano-silica content, reducing the inclusion volume fraction ξ increases the local concentration of particles inside the inclusions. This provides a direct mathematical representation of the fact that smaller nanoparticle-rich regions produce more severe local agglomeration.

In the first stage, the effective Young's modulus of each region is estimated by combining the Voigt and Reuss bounds with weights of 3/8 and 5/8, which accounts for randomly oriented reinforcement. Let E_m denote the Young's modulus of the concrete matrix and E_r the Young's modulus of the nano-silica reinforcement.

For the nanoparticle-rich inclusion region, the effective modulus is

$$E_{in} = \frac{3}{8\xi}[C_r\zeta E_r + (\xi - C_r\zeta)E_m] + \frac{5}{8}\left[\frac{\xi E_m E_r}{(\xi - C_r\zeta)E_r + C_r\zeta E_m}\right] \tag{11}$$

For the material outside the inclusions, the effective modulus is

$$E_{out} = \frac{3}{8}\left\{\frac{C_r(1-\zeta)}{1-\xi}E_r + \left[1 - \frac{C_r(1-\zeta)}{1-\xi}\right]E_m\right\} + \frac{5}{8}\left\{\frac{(1-\xi)E_r E_m}{[(1-\xi) - C_r(1-\zeta)]E_r + C_r(1-\zeta)E_m}\right\} \tag{12}$$

In the second stage, the agglomerates are treated as inclusions of volume fraction ξ embedded in the surrounding material, and the homogenized modulus is obtained from Paul's model [56], as follows:

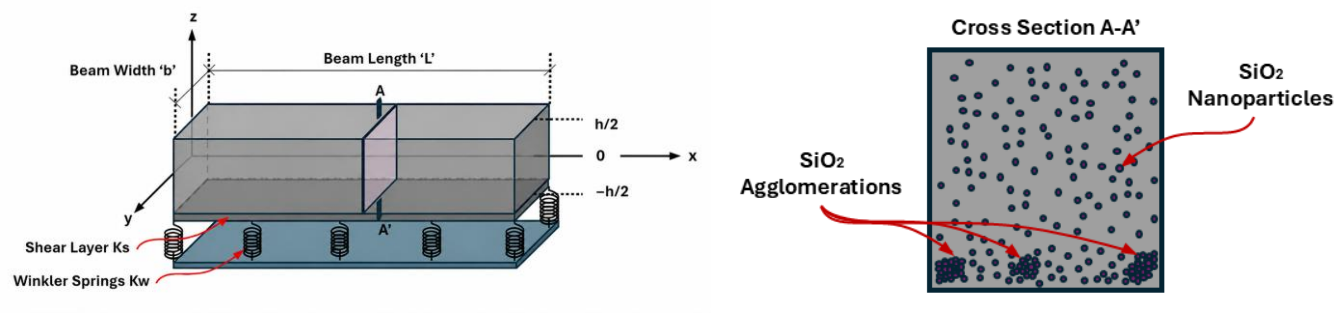
$$E_{hom} = E_{out}\left[\frac{E_{out} + (E_{in} - E_{out})\xi^{2/3}}{E_{out} + (E_{in} - E_{out})\xi^{2/3}(1 - \xi^{1/3})}\right] \tag{13}$$

Because the Reuss term of the first stage and the second stage are non-linear in ξ and ζ, the agglomeration parameters do not cancel, and E_{hom} depends on both of them. A pure two-stage Voigt average would make E_{hom} independent of ξ and ζ.

3. Mathematical Modeling of the Beam

3.1. Beam Theory

To establish the analytical model of the beam, the beam geometry and the associated Cartesian coordinate system are first defined, as shown in Figure 3. The longitudinal coordinate x is oriented along the beam axis and varies over $0 < x < L$, where L denotes the beam length. The transverse coordinate y is measured across the beam width and belongs to the interval $0 < y < b$. The coordinate z is measured through the beam thickness and varies between $-h/2$ and $h/2$, where b and h represent the beam width and thickness, respectively.



(**a**) (**b**)

Figure 3. Reinforced concrete beam on a two-parameter elastic foundation: (**a**) geometry of the beam and orientation of the Cartesian coordinate system, (**b**) transverse cross-section showing reinforcement distribution and agglomeration zones.

The kinematic assumptions adopted in this study are based on a higher-order shear deformation beam theory (NHSDT) formulated with only three (03) primary unknowns. The displacement field is therefore conveniently expressed as the superposition of a classical kinematic part $u^{(c)}(x,z)$, and a higher-order contribution $u^{(h)}(x,z)$. Accordingly, the total displacement vector $\Psi(x,z)$ is decomposed as

$$\Psi(x,z) = u^{(c)}(x,z) + u^{(h)}(x,z) \tag{14}$$

The classical component of the displacement field is defined by

$$u^{(c)}(x,z) = \begin{bmatrix} u_0(x) - z\dfrac{dw_0(x)}{dx} \\ w_0(x) \end{bmatrix} \tag{15}$$

The higher-order contribution is expressed as

$$u^{(h)}(x,z) = -k_1 f(z)\begin{bmatrix} \int \theta(x)\,dx \\ 0 \end{bmatrix} \tag{16}$$

Here, $u_0(x)$ and $w_0(x)$ denote the axial and transverse displacements of the reference axis, respectively; $\theta(x)$ represents the higher-order deformation variable; k_1 is a

shear-related coefficient and $f(z)$ is a prescribed thickness-dependent shape function, which is introduced as follows [29]:

$$f(z) = z - \frac{4z^3}{3h^2} \tag{17}$$

By differentiating the displacement field with respect to the spatial coordinates, the axial strain ε_{xx} and the shear strain γ_{xz} are obtained as functions of $u_0(x)$, $w_0(x)$, $\theta(x)$, and $f(z)$,

$$\begin{Bmatrix} \varepsilon_{xx} \\ \gamma_{xz} \end{Bmatrix} = \begin{Bmatrix} \frac{du_0}{dx} - z\frac{d^2w_0}{dx^2} - k_1 f(z)\theta(x) \\ -k_1 f'(z)\int \theta(x)\,dx \end{Bmatrix} \tag{18}$$

The constitutive relationship between the stress and strain components is written in matrix form as

$$\sigma(x,z) = \begin{bmatrix} \sigma_{xx} \\ \tau_{xz} \end{bmatrix} = \begin{bmatrix} Q_{11}^{mr} & 0 \\ 0 & Q_{55}^{mr} \end{bmatrix} \begin{Bmatrix} \varepsilon_{xx} \\ \gamma_{xz} \end{Bmatrix} \tag{19}$$

In this expression, Q_{11}^{mr} and Q_{55}^{mr} denote the effective axial and shear stiffness coefficients of the reinforced-concrete beam. These effective properties may be evaluated using the Voigt homogenization model, where the superscripts *m* and *r* identify the matrix and reinforcement contributions, respectively.

3.2. Equations of Motion

The governing equations of motion are derived by applying Hamilton's principle to the reinforced beam resting on a two-parameter elastic foundation. Hamilton's principle states that the time integral of the difference between the virtual kinetic energy and the virtual total potential energy must vanish over the time interval $[t_1, t_2]$, as follows:

$$\delta \int_{t_1}^{t_2} (\delta\aleph - \delta\chi)\, dt = 0 \tag{20}$$

The virtual variation in the total potential energy is defined as

$$\delta\aleph = \delta U_b + \delta U_f \tag{21}$$

where δU_b and δU_f representing the virtual variations in the internal strain energy of the beam and the strain energy of the elastic foundation, respectively, and $\delta\chi$ represents the virtual variation in the kinetic energy of the beam.

The virtual strain energy of the beam is given by

$$\delta U_b = \int_0^L \int_{-h/2}^{h/2} (\sigma_{xx}\,\delta\varepsilon_{xx} + \tau_{xz}\,\delta\gamma_{xz})\; dA\, dz \tag{22}$$

Here, σ_{xx} and τ_{xz} are the axial and shear stress components, while $\delta\varepsilon_{xx}$ and $\delta\gamma_{xz}$ are the corresponding virtual strain components. The limits of integration account for the beam length and thickness.

Substitution of the displacement field into Equation (22) gives

$$\delta U_b = \int_0^L \int_{-h/2}^{h/2} [\,\sigma_{xx}(\Psi)\,\delta\varepsilon_{xx}(\Psi) + \tau_{xz}(\Psi)\,\delta\gamma_{xz}(\Psi)]\, dA\, dz \tag{23}$$

where $\varepsilon_{xx}(\Psi)$ and $\gamma_{xz}(\Psi)$ are the axial and shear strains derived from the NHSDT displacement field $\Psi(x,z)$. Using the expressions for the axial and shear strains from the displacement field, the virtual strain energy of the beam can be written explicitly as

$$\delta U_b = \int_0^L \int_{-h/2}^{h/2} [\, Q_{11}^{mr}\left(\frac{du_0}{dx} - z\frac{d^2w_0}{dx^2} - k_1 f(z)\,\theta(x)\right)\left(\frac{d(\delta u_0)}{dx} - z\frac{d^2(\delta w_0)}{dx^2} - k_1 f(z)\,\delta\theta(x)\right) + Q_{55}^{mr}\left(-k_1 f'(z)\int \theta(x)\,dx\right)\left(-k_1 f'(z)\int \delta\theta(x)\,dx\right)]dz\,dx \tag{24}$$

By introducing the resultant stiffness coefficients, the contributions of the beam cross-section and the higher-order NHSDT terms can be represented in a compact form. Specifically, $N^{(c)}$ denotes the axial stiffness coefficient, $M^{(c)}$ the bending stiffness coefficient, $S^{(h)}$ the higher-order axial contribution due to the NHSDT term, and $P^{(h)}$ the shear contribution associated with the thickness-dependent shear deformation. These coefficients are defined as integrals through the beam thickness

$$N^{(c)} = \int_{-h/2}^{h/2} Q_{11}^{mr}\; dz \tag{25}$$

$$M^{(c)} = \int_{-h/2}^{h/2} z\; Q_{11}^{mr}\; dz \tag{26}$$

$$S^{(h)} = \int_{-h/2}^{h/2} f(z)\; Q_{11}^{mr}\; dz \tag{27}$$

$$P^{(h)} = \int_{-h/2}^{h/2} f'(z)\; Q_{55}^{mr}\; dz \tag{28}$$

Accordingly, the virtual strain energy of the beam can be expressed in compact form as

$$\delta U_b = \int_0^L \Bigg[\underbrace{N^{(c)}\frac{du_0}{dx}\frac{d(\delta u_0)}{dx}}_{axial\ deformation} + \underbrace{M^{(c)}\left(\frac{d^2w_0}{dx^2}\frac{d^2(\delta w_0)}{dx^2} + \frac{du_0}{dx}\frac{d^2(\delta w_0)}{dx^2} - \frac{d^2w_0}{dx^2}\frac{d(\delta u_0)}{dx}\right)}_{\text{bending contribution}} + \underbrace{S^{(h)}\left(-\theta\frac{d(\delta u_0)}{dx} + \theta\frac{d^2(\delta w_0)}{dx^2} + \frac{du_0}{dx}\delta\theta - \frac{d^2w_0}{dx^2}\delta\theta + k_1\theta\delta\theta\right)}_{\text{higher-order NHSDT contribution}} + \underbrace{P^{(h)}k_1\int \theta(x)dx\int \delta\theta(x)dx}_{\text{shear contribution}} \Bigg] dx \tag{29}$$

The stress resultants are subsequently expressed in terms of the primary displacement variables and the effective stiffness coefficients. These resultants account for the contributions of axial deformation, bending, higher-order deformation, and shear deformation, as follows:

$$N^{(c)} = k_1\, F_{11}\,\theta(x,y,t) - A_{11}\,\frac{\partial^2 w_0(x,y,t)}{\partial x^2} + Y_s\,\frac{\partial u_0(x,y,t)}{\partial x} \tag{30}$$

$$M^{(c)} = k_1\, F_{z11}\,\theta(x,y,t) - B_{11}\,\frac{\partial^2 w_0(x,y,t)}{\partial x^2} + A_{11}\,\frac{\partial u_0(x,y,t)}{\partial x} \tag{31}$$

$$S^{(h)} = k_1\, K_{z11}\,\theta(x,y,t) - F_{z11}\,\frac{\partial^2 w_0(x,y,t)}{\partial x^2} + F_{11}\,\frac{\partial u_0(x,y,t)}{\partial x} \tag{32}$$

$$P^{(h)} = k_1\, A_p\, V_{z55}\,\frac{\partial \theta(x,y,t)}{\partial x} \tag{33}$$

The sectional stiffness coefficients appearing in Equations (30–33) are defined as

$$F_{11} = \int_{-h/2}^{h/2} Q_{11}^{mr}(z) f(z)\, dz \tag{34}$$

$$A_{11} = -\int_{-h/2}^{h/2} Q_{11}^{mr}(z) z\, dz \tag{35}$$

$$K_{z11} = \int_{-h/2}^{h/2} Q_{11}^{mr}(z) f^2(z)\, dz \tag{36}$$

$$V_{z55} = \int_{-\frac{h}{2}}^{\frac{h}{2}} Q_{55}^{mr}(z) \left(\frac{df(z)}{dz}\right)^2 dz \tag{37}$$

$$F_{z11} = \int_{-h/2}^{h/2} z\ Q_{11}^{mr}(z) f(z)\, dz \tag{38}$$

$$B_{11} = \int_{-h/2}^{h/2} Q_{11}^{mr}(z) z^2\, dz \tag{39}$$

$$Y_{s11} = \int_{-h/2}^{h/2} Q_{11}^{mr}(z)\, dz \tag{40}$$

The virtual strain energy of the two-parameter elastic foundation consists of two contributions: the Winkler foundation component, which provides a restoring force proportional to the local transverse displacement, and the Pasternak component, which accounts for shear interaction between adjacent points of the foundation. Thus,

$$\delta U_f = \int_0^L \left[K_w\, w_0(x,y,t)\, \delta w_0(x,y,t) + K_s \frac{\partial w_0(x,y,t)}{\partial x} \frac{\partial \delta w_0(x,y,t)}{\partial x}\right] dx \tag{41}$$

The Winkler foundation coefficient is defined as

$$K_w = \frac{\beta_w A_{110}}{L^2} \tag{42}$$

where β_w is the Winkler foundation parameter and A_{110} is the extension stiffness of a homogeneous beam made entirely of the matrix material.

The Pasternak shear-layer coefficient is defined as

$$K_s = \beta_s A_{110} \tag{43}$$

where β_s is the shear-layer parameter. The quantity $\delta w_0(x,y,t)$ denotes the virtual transverse displacement. The parameters β_w and β_s characterize the normal springs and the shear layer, respectively.

The Winkler and Pasternak coefficients have different physical dimensions.

K_w is a subgrade reaction modulus, whereas K_s characterizes the shear stiffness of the foundation layer. Therefore, their relative contributions to the natural frequency cannot be assessed by comparing their dimensional values directly. In the nondimensional formulation, both coefficients are normalized by the same reference flexural stiffness of the beam and the appropriate powers of the beam length, so that the resulting parameters represent the relative importance of the local Winkler restoring force and the Pasternak shear-coupling mechanism in the beam–foundation system.

The virtual variation in the kinetic energy of the beam is expressed as

$$\delta\chi = \int_0^L \int_{-h/2}^{h/2} \rho^{mr}(z)\big[\big(\dot{u}_0(x,t) - z\,\dot{w}_0(x,t) - k_1 f(z)\,\dot{\theta}(x,t)\big)\,\delta\big(\dot{u}_0(x,t) - z\,\dot{w}_0(x,t) - k_1 f(z)\,\dot{\theta}(x,t)\big) + \dot{w}_0(x,t)\,\delta\dot{w}_0(x,t)\big)\big]dA\,dz\,dx \tag{44}$$

Here, $\rho^{mr}(z)$ denotes the mass-density distribution through the homogenized beam thickness, and an overdot indicates differentiation with respect to time. The functions $u_1(x,z,t)$ and $u_3(x,z,t)$ represent the axial and transverse displacement components associated with the adopted NHSDT kinematics.

For convenience, the following mass-related coefficients are introduced:

$$I_0 = \int_{-h/2}^{h/2} \rho(z)\,dz \tag{45}$$

$$I_1 = \int_{-h/2}^{h/2} \rho(z)\,z\,dz \tag{46}$$

$$J_0 = \int_{-h/2}^{h/2} \rho(z)\,f(z)\,dz \tag{47}$$

The coefficient I_0 represents the total mass per unit length of the beam. The coefficient I_1 is the first mass moment about the reference or neutral axis and describes the inertial coupling between axial and transverse motions. The coefficient J_0 represents the mass contribution associated with the higher-order deformation variable θ.

Using these coefficients, the virtual kinetic energy can be written in a reduced form as

$$\delta\chi = \int_0^L [\,I_0\,\dot{w}_0\,\delta\dot{w}_0 + I_0\,\dot{u}_0\,\delta\dot{u}_0 - I_1\,\dot{w}_0\,\delta\dot{u}_0 - I_1\,\dot{u}_0\,\delta\dot{w}_0 - k_1 J_0\,\dot{\theta}\,\delta\dot{u}_0]dx \tag{48}$$

Substitution of Equations (29), (41) and (44) into Hamilton's principle, followed by the application of integration by parts and collection of the coefficients associated with the independent variations u_0, w_0, and θ, yields the governing equations of motion:

$$\delta u_0 : \frac{\partial N^{(c)}}{\partial x} = I_0\,\ddot{u}_0 - I_1\,\ddot{w}_0 - k_1 J_0\,\ddot{\theta} \tag{49}$$

$$\delta w_0 : \frac{\partial^2 M^{(c)}}{\partial x^2} - K_w w_0 + K_s \nabla^2 w_0 = I_0\,\ddot{w}_0 - I_1\,\ddot{u}_0 \tag{50}$$

$$\delta\theta : -k_1 A' \frac{\partial^2 S^{(h)}}{\partial x^2} + k_1 A' \frac{\partial P^{(h)}}{\partial x} = k_1 J_0\,\ddot{u}_0 \tag{51}$$

For compactness, the following parameters are introduced:

$$A' = -\frac{1}{\alpha^2}\,, \qquad k_1 = \alpha^2 \tag{52}$$

3.3. Closed Form Solutions

The analytical solution for the reinforced beam is obtained using Navier's method. The displacement variables are expanded as trigonometric series selected to satisfy the boundary conditions at the beam ends. The assumed harmonic displacement fields are

$$u_0(x,t) = \sum_{n=1}^{\infty} U_n(t)\,\frac{dX(x)}{dx}\,e^{i\omega t} \tag{53}$$

$$w_0(x,t) = \sum_{n=1}^{\infty} W_n(t)\, X(x) e^{i\omega t} \tag{54}$$

$$\theta(x,t) = \sum_{n=1}^{\infty} \Theta_n(t)\ \frac{dX(x)}{dx} e^{i\omega t} \tag{55}$$

Here, U_n, W_n, and Θ_n are the generalized modal amplitudes to be determined. The quantity ω is the natural angular frequency associated with the mode under consideration, and $i = \sqrt{-1}$ is the imaginary unit used to represent harmonic motion in the frequency domain.

The free-vibration behavior of the reinforced concrete beam is investigated under three boundary configurations: simply supported (S–S), clamped–clamped (C–C), and clamped–simply supported (C–S). These configurations represent different levels of end restraint and are considered to evaluate their influence on the dimensionless natural frequencies. Table 1 summarizes the corresponding boundary conditions and the assumed spatial functions adopted in the analytical formulation.

Table 1. Boundary conditions and assumed functions [57].

Boundary Condition	Conditions	$X(x)$
S-S	$w_0 = 0$ and $M = 0$ at $x = 0$ and L	$\sin(\lambda x)$
C-C	$u_0 = w_0 = w_0{}' = \varphi = 0$ at $x = 0$ and L	$1 - \cos(2\lambda x)$
C-S	$u_0 = w_0 = w_0{}' = \varphi = 0$ at $x = 0$; $w_0 = 0$ and $M = 0$ at $x = L$	$\sin(\lambda x)(\cos(2\lambda x) - 1)$

After substituting the assumed trigonometric expansions into the governing equations and collecting the coefficients of the corresponding modal terms, the resulting algebraic system can be written as this generalized eigenvalue problem:

$$\Phi\, X = \omega^2\, \Upsilon\, X \tag{56}$$

In this equation, Φ is the stiffness matrix, Υ is the mass matrix, and

$$X = \begin{Bmatrix} U_n \\ W_n \\ \Theta_n \end{Bmatrix} \tag{57}$$

is the vector of generalized modal amplitudes. The eigenvalues ω^2 provide the squared natural frequencies of the beam, while the associated eigenvectors describe the corresponding mode shapes.

The stiffness matrix Φ represents the structural stiffness of the reinforced beam together with the restoring effects introduced by the two-parameter elastic foundation. It is expressed as

$$\Phi = \begin{bmatrix} \Phi_{11}^{(c)} & \Phi_{12}^{(c)} & \Phi_{13}^{(h)} \\ \Phi_{12}^{(c)} & \Phi_{22}^{(c)} & \Phi_{23}^{(h)} \\ \Phi_{13}^{(h)} & \Phi_{23}^{(h)} & \Phi_{33}^{(h)} \end{bmatrix} = \begin{bmatrix} -Y_{s11}\alpha^2 & A_{11}\alpha^3 & F_{11}k_1\alpha \\ A_{11}\alpha^3 & -B_{11}\alpha^3 & -F_{z11}k_1\alpha^2 \\ F_{11}k_1\alpha & -F_{z11}k_1\alpha^2 & -A'^2 V_{z55}{k_1}^2\alpha^2 - K_{z11}{k_1}^2 \end{bmatrix} \tag{58}$$

The mass matrix Υ represents the inertial properties of the beam. It includes the inertia associated with axial motion, transverse motion, and the higher-order deformation variable. Each entry Υ_{ij} describes the inertial coupling between the i-th and j-th generalized coordinates. For the m-th mode, the mass matrix is given by

$$\Upsilon = \begin{bmatrix} \Upsilon_{11}^{(c)} & \Upsilon_{12}^{(c)} & \Upsilon_{13}^{(h)} \\ \Upsilon_{12}^{(c)} & \Upsilon_{22}^{(c)} & \Upsilon_{23}^{(h)} \\ \Upsilon_{13}^{(h)} & \Upsilon_{23}^{(h)} & \Upsilon_{33}^{(h)} \end{bmatrix} = \begin{bmatrix} I_0 & -I_1 & -k_1 J_0 \\ -I_1 & I_0 & 0 \\ -k_1 J_0 & 0 & k_1^2 V_{z55} \end{bmatrix}, \tag{59}$$

The negative diagonal terms appearing in the stiffness matrix are associated with the sign convention adopted for the third governing equation, which corresponds to the higher-order kinematic variable. They do not indicate a physical instability. The generalized eigenvalue problem is solved consistently in the form $(\Phi - \omega^2 \Upsilon)X = 0$, and all eigenvalues obtained for the configurations considered are positive, yielding physically meaningful natural frequencies. The positive definiteness of the mass matrix and the positivity of the computed eigenvalues were verified numerically.

4. Results and Discussion

4.1. Verification of the Beam Model

To verify the formulation and the Navier solution of the present beam model, the results are compared with published solutions for functionally graded beams. The verification is carried out independently of the nanoparticle homogenization of Section 2.2, because no published results exist for the complete problem of agglomerated SiO_2-reinforced concrete beams on an elastic foundation.

The higher-order kinematics are verified first, for a thick beam without foundation. Jia et al. [58] computed the fundamental frequency of simply supported (S-S) functionally graded beams with Reddy's third-order shear deformation theory and compared it with the results of Şimşek [59], who used several higher-order beam theories. The beam is made of aluminium (E_m = 70 GPa, φ_m = 2702 Kg/m^3) and alumina (E_c = 380 GPa, φ_c = 3960 Kg/m^3), with a constant Poisson's ratio of 0.3 and a power-law variation in the ceramic volume fraction through the thickness, of index p. The case p = 0 corresponds to a homogeneous alumina beam. The span-to-thickness ratio is L/h = 5, for which shear deformation has a strong effect. The through-thickness variations in the Young's modulus, density and shear modulus enter the stiffness and mass coefficients of Equations (25–28), (34–40) and (45–47). The results are given in Table 2.

Table 2. Verification of the fundamental frequency $\hat{\omega}$ of a simply supported Al/Al_2O_3 beam without foundation, L/h = 5.

Beam Theory	Power Law Index "p"	0	0.2	1	10
CBT	Present	0.21933	0.20408	0.16884	0.14236
FSDT (X_s = 5/6)	Present	0.20610	0.19222	0.15961	0.13254
NHSDT	Present	0.20611	0.19232	0.15962	0.13126
NHSDT	Jia et al. [58]	0.20611	0.19232	0.15962	0.13126
HSDT	Şimşek [59]	0.20611	0.19237	0.15962	0.13126

The foundation terms are verified next against the results of Jia et al. [58], who analysed simply supported functionally graded beams on a Winkler–Pasternak foundation with Reddy's third-order shear deformation theory. Their foundation results are presented graphically. The values of the undamped fundamental and higher frequencies are read from their figures for a beam with p = 1 and L/h = 20, for two foundation stiffness combinations, and are therefore accurate to within about 2%. Their frequency parameter is normalized by the properties of alumina, and the foundation parameters by the bending rigidity of the alumina section. The reference values are converted to the dimensionless frequency of the present study, using the properties of aluminium as reference, and the foundation parameters are converted to the coefficients β_w and β_s of the present model, so that the comparison is made on the same physical beam and foundation. The comparison is given in Table 3.

Table 3. Verification of the dimensionless frequency $\tilde{\omega}$ of a simply supported Al/Al_2O_3 beam (p = 1, L/h = 20) on a Winkler–Pasternak foundation.

Mode	Winkler-Pasternak Elastic Foundation	Jia et al. [58]	Present NHSDT
1	$K_w = 25$, $K_p = 5$	0.0167	0.0166
2	$K_w = 100$, $K_p = 10$	0.0242	0.0242
3	$K_w = 100$, $K_p = 10$	0.0539	0.0540
4	$K_w = 100$, $K_p = 10$	0.1035	0.1036

Table 3 compares the present frequencies with those read from the figures of Jia et al. [58] for a simply supported Al/Al_2O_3 beam with $p = 1$ and $L/h = 20$ on a Winkler–Pasternak foundation. The reference results show that the fundamental frequency rises from 0.0167 to 0.0242 when the foundation stiffness is increased from $K_w = 25$, $K_p = 5$ to $K_w = 100$, $K_p = 10$, and that the frequencies increase strongly with the mode number, reaching 0.0539 for the second mode and 0.1035 for the third mode on the stiffer foundation. The present results reproduce both trends, with a maximum difference of 0.6% from the reference values. Since the reference values are read from graphs, which limits their accuracy to about 2%, differences in this order are not significant, and the agreement confirms that the Winkler and Pasternak foundation terms and the third-order shear kinematics of the present model are correctly implemented for a beam of moderate slenderness.

4.2. Effects of Agglomeration, Slenderness and Foundation Stiffness

The agreement obtained in Section 4.1 shows that the higher-order beam formulation, the foundation terms and the Navier solution reproduce published results for functionally graded beams, both without foundation and on a Winkler–Pasternak foundation. The formulation is now applied to the problem that motivates this work: the free vibration of concrete beams reinforced with SiO_2 nanoparticles, in which the effective stiffness is governed by the nanoparticle content and by the agglomeration state described by the parameters ξ and ζ. The effects of the SiO_2 volume fraction, the agglomeration parameters, the slenderness ratio, the beam theory and the Winkler and Pasternak foundation coefficients on the dimensionless natural frequency are examined in the following. The computational program verified in Section 4.1 is employed for the numerical investigation. A concrete beam is considered, with a matrix elastic modulus $E_m = 20$ GPa and density $\rho_m = 2500$ Kg/m^3, reinforced by SiO_2 nanoparticles characterized by an elastic modulus $E_r = 70$ GPa and density $\rho_r = 2334$ Kg/m^3. The matrix modulus represents a normal-strength concrete at a fixed mix proportion and curing state, whereas the nanoparticle modulus is a representative value for amorphous silica. These material properties are adopted to investigate parametric trends rather than to predict the response of a specific commercial mixture. Because the effective stiffness of the nanoparticle phase and its interphase depends on particle size, surface chemistry, dispersion, degree of reaction, and curing age, experimental calibration would be required for mixture-specific predictions.

The following dimensionless properties are used in presenting the numerical results in graphical forms for vibration analysis:

$$\widehat{\omega} = \omega h \sqrt{\frac{\rho_m}{E_m}} \tag{60}$$

The influence of the agglomeration parameters ζ and ξ on the effective Young's modulus, as a function of the nano-silica volume fraction, is plotted in Figures 4 and 5. In the two-parameter micromechanical model adopted here, the nanoparticles are assumed to form spherical clusters embedded in the matrix: ξ is the volume fraction of the nanoparticle-rich inclusions and ζ is the fraction of the nanoparticles located inside them (Equations (4–5)). Uniform dispersion corresponds to $\zeta = \xi$, and agglomeration increases as ζ exceeds ξ. Figure 4 considers the limiting case $\xi = 1$, in which the nanoparticle-rich phase

occupies the entire representative volume element. In this degenerate limit, the two-region partition of Equations (4)–(10) is no longer applicable because no distinct matrix region exists outside the inclusion. Therefore, ζ is not interpreted as the fraction of nanoparticles located inside a separate agglomerated region, but as the fraction of the nominal nano-SiO_2 content that is effectively incorporated into the load-transferring solid phase. The remaining fraction (1 − ζ)Cr represents inactive or poorly bonded nanoparticle material that does not contribute to the effective stiffness. Accordingly, the effective Young's modulus in Figure 4 is evaluated using the single-phase Voigt mixture

$$E_{hom} = E_m\ (1 - C_r\ \zeta) + E_r\ (C_r\ \zeta) \quad (61)$$

with the admissibility condition $0 \le Cr\zeta \le 1$. For all cases considered, $Cr \le 0.20$; hence the full range $0 \le \zeta \le 1$ is physically permissible.

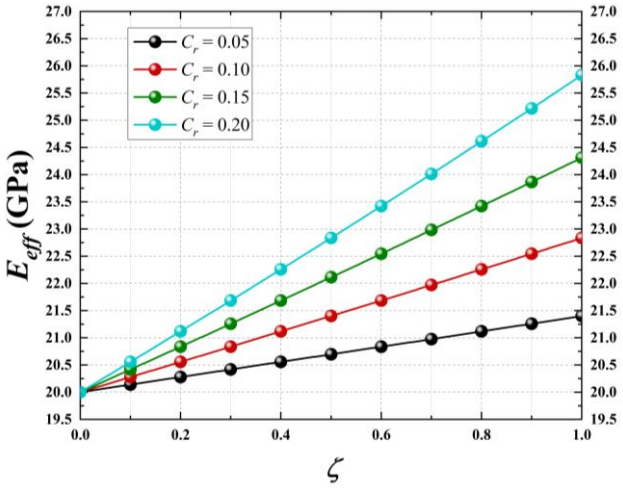


Figure 4. Effect of the effective nano-SiO_2 participation parameter ζ on the effective elastic modulus in the limiting one-phase case ξ = 1. Here, ζ denotes the fraction of the nominal nanoparticle content that actively contributes to load transfer; the remaining fraction is treated as inactive.

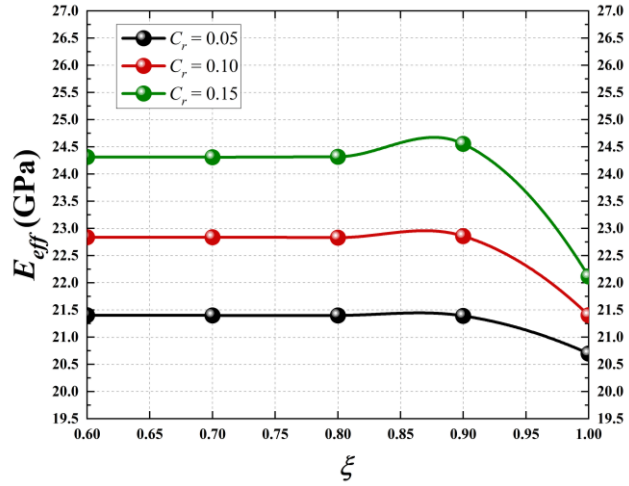


Figure 5. Effect of nano SiO_2 agglomeration on the effective elastic modulus with ζ = 0.5.

Figure 5 presents the more general case, for a fixed value of ζ = 0.5, in which both agglomeration parameters, ζ and ξ, are varied to fully describe the agglomeration state of the nano-SiO_2 particles. For a given ζ, decreasing ξ concentrates a larger share of the total nanoparticle volume into the cluster regions, converting what would otherwise be well-distributed stiff inclusions into isolated, particle-rich cores surrounded by a nanoparticle-

depleted matrix. Since the reinforcing action of a filler is governed primarily by the continuity of the particle-matrix interface, rather than by the intrinsic stiffness of the filler alone, this redistribution systematically lowers the effective modulus for any fixed total nanoparticle content. The results confirm that nanoparticle agglomeration exerts a pronounced detrimental effect on the effective elastic properties of the reinforced beam, underscoring that the quality of nanoparticle dispersion, and not the nanoparticle content alone, governs the mechanical benefit of nano-reinforcement.

The nanoparticle volume fraction *Cr* is defined with respect to the total volume of the homogenized solid composite. It should not be confused with the common practical dosage expressed as a percentage by mass of cement or binder. For a given mix design, the binder-based mass dosage can be converted to *Cr* using the densities and volumes of cement, aggregates, water, and nano-SiO_2. The upper bound *Cr* is used as a parametric limit to examine the sensitivity of the homogenized response and is not proposed as a recommended practical dosage.

The effect of nanoparticle agglomeration on the dimensionless frequency of the beam, as a function of the volume fraction of SiO_2 nanoparticles, is illustrated in Figures 6 and 7. Since the natural frequency of a vibrating beam scales with the square root of the ratio between its effective bending stiffness and its mass, the lower frequency obtained when agglomeration is taken into account is a direct dynamic consequence of the stiffness reduction discussed above: nanoparticle clustering lowers the effective elastic modulus of the reinforced concrete without a corresponding reduction in mass, so the stiffness-to-mass ratio, and hence the frequency, decreases relative to the ideally dispersed case. Conversely, the frequency increases with increasing nano-SiO_2 concentration for both models, because a higher nanoparticle content raises the effective stiffness of the composite; the increase in the frequency with the SiO_2 content is caused almost entirely by the stiffening of the composite. In the present model the density changes little: for the largest content considered (C_r = 0.20) the mass density decreases by only 1.3%, which contributes about 0.7% to the frequency, whereas the increase of the effective modulus contributes about 14%. The effect of the density depends on the density assumed for the nano-silica and on the mix design, and is not a distinguishing feature of this reinforcement.

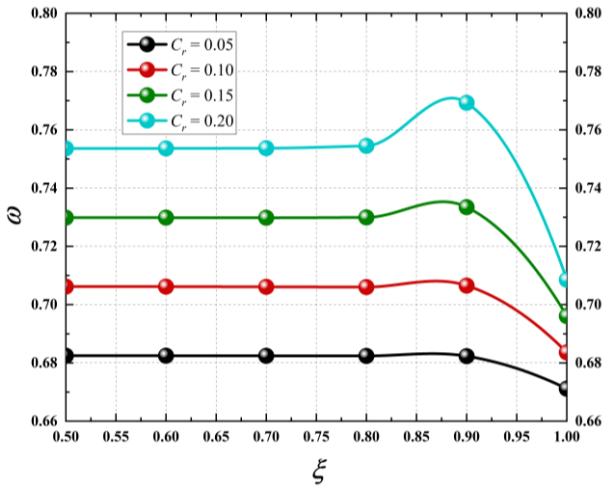


Figure 6. Agglomeration effect on the dimensionless frequency of reinforced concrete beam (*L*/*h* = 5, $\beta_W = \beta_S = 0$, $\zeta = 0.5$).

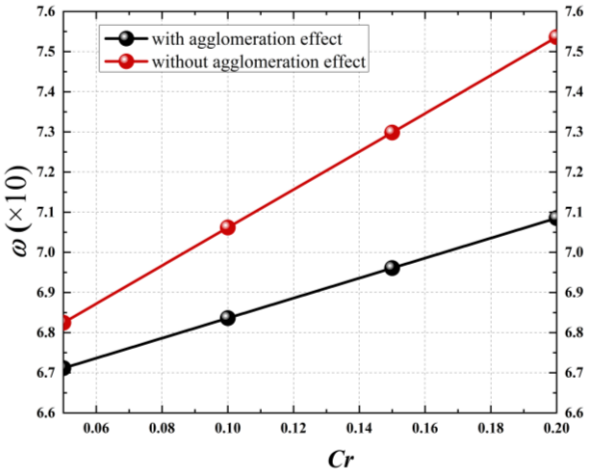


Figure 7. Agglomeration effect on the dimensionless frequency of reinforced concrete beam (L/h = 5, $\beta_W = \beta_S = 0$).

Figure 8 presents the effect of the length-to-thickness ratio L/h on the dimensionless natural frequency of the reinforced concrete beam for several nano-SiO_2 volume fractions, with $\xi = \zeta = 0.5$. For a fixed beam length, increasing L/h corresponds to reducing the beam thickness and therefore increasing the beam slenderness. Beams with higher nanoparticle volume fractions exhibit higher frequency values, owing to their greater effective elastic modulus. In contrast, the dimensionless natural frequency decreases as L/h increases. This trend arises because, at a fixed length, a smaller thickness reduces both the cross-sectional moment of inertia and the mass per unit length; however, the reduction in flexural stiffness dominates, leading to a lower stiffness-to-mass ratio and hence a lower natural frequency. The sensitivity to L/h is most pronounced in the moderately thick range, approximately L/h = 5–15, where transverse shear deformation remains significant. For larger values of L/h, the frequency decreases more gradually as the beam approaches the slender, shear-insensitive limit.

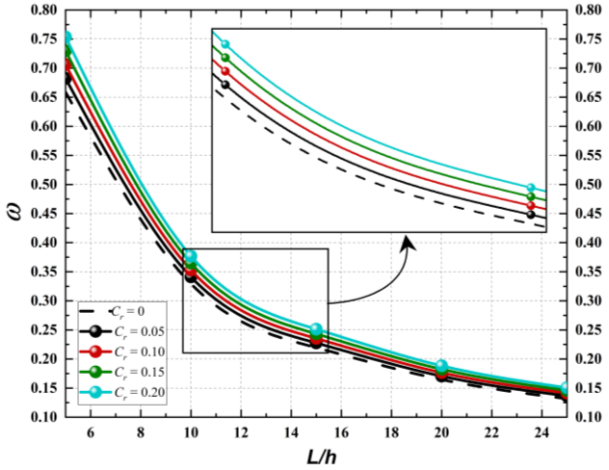


Figure 8. Effect of the length-to-thickness ratio L/h on the dimensionless natural frequency of the reinforced concrete beam for various nano-SiO_2 volume fractions ($\xi = \zeta = 0.5$).

For comparison purposes, Figure 9 illustrates the influence of different beam theories on the predicted natural frequencies of the concrete beam. Because the FSDT assumes a transverse shear strain that is uniform across the beam thickness, whereas the true through-thickness shear strain predicted by elasticity theory, and captured directly by the NHSDT through its higher-order displacement field, is parabolic and vanishes at the free

surfaces, a shear correction factor X_s is introduced to compensate for this simplification, matching the strain energy of the assumed uniform shear-strain state to that of the true parabolic distribution. It is evident that adopting X_s = 5/6 in the first-order theory, the value obtained from this energy-equivalence condition for a rectangular cross-section, yields results in very good agreement with the NHSDT, whereas a correction factor of X_s = 1/2 corresponds to a cruder estimate of the shear stiffness and therefore underestimates the frequency values; this discrepancy diminishes, and the results approach those of the NHSDT, as the slenderness ratio increases, because the relative contribution of transverse shear deformation to the total deformation energy shrinks as the beam becomes more slender, so the choice of correction factor becomes progressively less influential. These findings confirm that, when the appropriate shear correction factor χs = 5/6 is used, the FSDT predictions agree closely with the NHSDT results over the considered range of L/h. It should be emphasized that the natural frequency itself remains strongly dependent on L/h, since increasing slenderness reduces the beam's flexural stiffness-to-mass ratio. What becomes nearly independent of L/h is the relative difference between the FSDT (χs = 5/6) and NHSDT predictions: as L/h increases, transverse shear deformation contributes less to the total strain energy, so the difference between the two theories diminishes. By contrast, FSDT with χs = 1/2 underestimates the shear stiffness and therefore produces a more noticeable deviation from the NHSDT results, particularly for lower L/h values, where shear deformation is more significant. The comparison with FSDT is intended as an internal consistency check of the higher-order kinematics, whereas the independent verification of the beam formulation and foundation terms is provided in Section 4.1 through comparison with the analytical results of Jia et al. for functionally graded beams on elastic foundations.

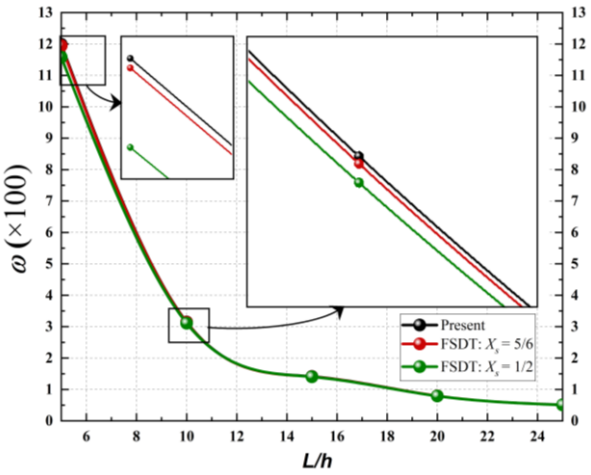


Figure 9. Dimensionless frequency of reinforced concrete beams reinforced with nano silica under different theories ($\xi = \zeta = 0.5$).

Figure 10 illustrates the variation in the dimensionless fundamental frequency with silica-particle volume fraction for concrete beams under simply supported (SS), clamped-clamped (CC), and clamped-simply supported (CS) boundary conditions, considering a slenderness ratio of (L/h = 5) and fixed agglomeration parameters ($\xi = \zeta = 0.5$). For all three boundary configurations, the dimensionless frequency increases monotonically as the silica-particle volume fraction rises from 0 to 0.20, exhibiting an approximately linear trend over the investigated range. The frequency increases by approximately 14.4% for each boundary condition, indicating a consistent reinforcement-induced modification of the dynamic response. This behavior reflects the combined influence of silica-particle

incorporation on the effective elastic properties and mass density of the composite, as described by the two-stage homogenization model.

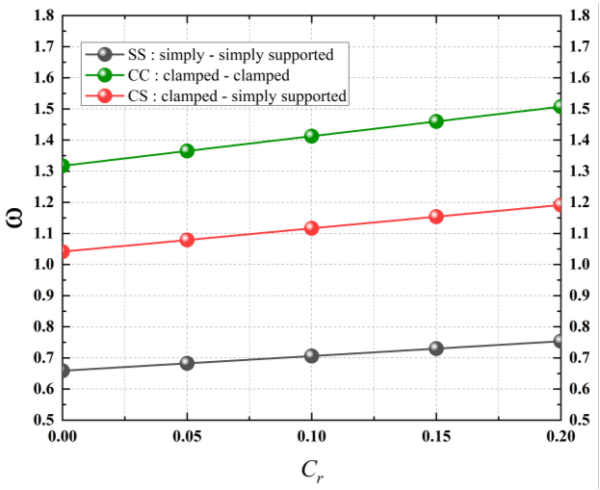


Figure 10. Variation in the dimensionless fundamental frequency with silica-particle volume fraction for different boundary conditions at (L/h = 5), with fixed agglomeration parameters ($\xi = \zeta = 0.5$).

The results further demonstrate the significant influence of boundary restraints on the fundamental frequency, with the clamped-clamped configuration exhibiting the highest values, followed by the clamped-simply supported and simply supported configurations. This hierarchy is consistent with the increasing kinematic constraints imposed on the beam, which enhance its effective structural stiffness. The nearly identical relative frequency increments across the three configurations suggest that the effect of silica-particle content remains approximately proportional to the baseline frequency within the investigated range. Since the agglomeration parameters are maintained constant, these results isolate the influence of silica-particle volume fraction for a prescribed agglomeration state rather than quantifying the independent effects of agglomeration.

Figure 11 shows the variation in the dimensionless natural frequency with the dimensionless Winkler and Pasternak foundation parameters. Because these parameters are nondimensionalized using the same reference beam stiffness and length scales, their values can be compared on a consistent basis. For the range of dimensionless foundation stiffness considered, an increase in the Pasternak parameter produces a larger increase in the dimensionless natural frequency than an equal increase in the Winkler parameter. This trend reflects the different deformation mechanisms activated by the two foundation components: the Winkler component resists local transverse deflection, whereas the Pasternak component resists the gradient of deflection and therefore interacts directly with the curvature-dominated deformation field of a vibrating beam. Since beam vibration modes are governed primarily by bending curvature, the Pasternak shear-coupling term can contribute more efficiently to the overall stiffness-to-mass ratio than the local Winkler term over the investigated parameter range.

Physically, the Winkler term adds a distributed elastic foundation stiffness proportional to the local deflection, while the Pasternak term adds a stiffness contribution proportional to the second derivative of the deflection. Because the modal deflection of a simply supported beam varies sinusoidally, its curvature is of the same sinusoidal form but scaled by $(n\pi/L)^2$, consequently, the Pasternak contribution becomes increasingly important for higher vibration modes and shorter wavelengths.

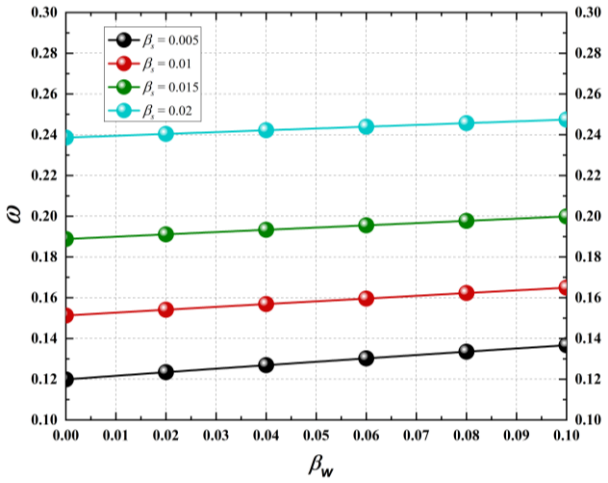


Figure 11. Dimensionless frequency of reinforced concrete beam with different variations on spring constant (L/h = 5, Cr = 0.10).

The present framework isolates the mechanical effect of nanoparticle dispersion and agglomeration on the elastic stiffness and free-vibration response of a nano-SiO_2 -modified concrete beam. It does not simulate the coupled chemo-mechanical evolution of the cementitious matrix. In real concrete, nano-SiO_2 may increase stiffness not only through its intrinsic elastic stiffness but also through pozzolanic C-S-H formation, hydration modification, pore refinement, and improvement of the interfacial transition zone. These mechanisms can make the experimentally observed stiffness gain larger or smaller than the purely elastic homogenization estimate, depending on dosage, dispersion method, water-to-binder ratio, cement replacement level, and curing age.

Consequently, the predicted frequencies should be interpreted as trends for a fixed matrix and hydration state. For practical design, the matrix modulus should be measured, or predicted using a hydration model, for the specific nano-SiO_2 -modified mixture and curing age. The present model is best viewed as a structural-scale tool that quantifies how a given effective stiffness, once determined experimentally or through a multiscale chemo-mechanical model, is translated into beam vibration response under different agglomeration states, slenderness ratios, and foundation conditions.

5. Conclusions, Limitations and Future Research Directions

5.1. Conclusions

This study developed a closed-form analytical framework for the free vibration of SiO_2 nanoparticle-reinforced concrete beams resting on a two-parameter Winkler–Pasternak elastic foundation, explicitly accounting for nanoparticle agglomeration through a Voigt-Reuss-Paul two-stage homogenization scheme (ξ, ζ). Beam kinematics were described using a higher-order shear deformation theory (NHSDT) that satisfies zero-traction conditions at the beam surfaces without a shear correction factor, and the governing equations, derived via Hamilton's principle, were solved in closed form using Navier's method for different boundary conditions. The results refer to an idealized two-phase representation of nano-silica-modified concrete at a fixed matrix and hydration state, and should be read as trends in the response and not as predictions for a specific mix. The main findings can be summarized as follows:

- The dimensionless natural frequency increases consistently with the SiO_2 volume fraction, but nanoparticle agglomeration systematically degrades this stiffening effect; for $\zeta < 0.4$ the reinforcement contribution becomes practically negligible.

- Maximum reinforcement efficiency, and the corresponding peak effective elastic modulus, is achieved when the agglomeration parameters are equal ($\zeta = \xi = 0.5$), that is when nanoparticle distribution inside and outside the cluster regions is essentially uniform.
- The Pasternak shear-layer coefficient exerts a markedly stronger influence on the natural frequency than the Winkler modulus, reflecting the former's coupling to beam curvature rather than local deflection alone.
- The dimensionless natural frequency decreases with increasing length-to-thickness ratio L/h, with the strongest variation occurring in the moderately thick range L/h = 5–15. The difference between the NHSDT and FSDT predictions with χs = 5/6 decreases as L/h increases, reflecting the reduced relative contribution of transverse shear deformation in slender beams.
- The boundary conditions significantly affect the fundamental frequency, with the CC configuration exhibiting the highest values, followed by CS and SS. This hierarchy reflects the increasing constraints on beam deformation, which enhance structural stiffness and raise the natural frequency.
- Benchmarking against first-order shear deformation theory (FSDT) confirmed that a shear correction factor of X_s = 5/6 reproduces the NHSDT frequencies with excellent accuracy, whereas X_s = 1/2 leads to a consistent underestimation, validating the reliability of the proposed higher-order formulation.

Collectively, these results demonstrate that the quality of nanoparticle dispersion, not merely the nanoparticle content, governs the dynamic performance of nano-engineered concrete beams, and that foundation type and beam geometry must be considered jointly with agglomeration state in design.

5.2. Limitations

- The effective elastic properties were obtained with a semi-empirical two-stage scheme (a Voigt–Reuss combination followed by Paul's model), which does not explicitly capture interfacial debonding, imperfect bonding, or particle–particle contact mechanics.
- Nanoparticles and agglomerates were idealized as isotropic and spherical. Actual agglomerate morphology and size distribution in cementitious matrices are more irregular.
- The nano-silica is modelled as an elastic reinforcing phase defined by its volume fraction in the homogenized solid. Porosity, packing density, the pozzolanic reaction, the formation and structure of C-S-H gel, the change in the degree of hydration and the partial replacement of cement are not modelled, and the density of the mixture follows the rule of mixtures.
- The formulation is restricted to linear elasticity and small deformations. Material nonlinearity, micro-cracking, and time-dependent effects (creep, shrinkage, curing-age evolution) were not considered.
- The Winkler–Pasternak foundation was treated as linear, elastic, and time-invariant, without foundation damping or nonlinear soil–structure interaction.
- The analysis is limited to free (undamped) vibration. Forced vibration, structural damping, and dynamic loading (moving loads, seismic excitation) were outside the present scope.
- No experimental validation was performed.

5.3. Future Research Directions

Several extensions of the present work are worth pursuing. The framework can be extended to other geometries using numerical approaches such as the Ritz method,

differential quadrature or finite elements, where closed-form Navier solutions are unavailable. The homogenization can be refined in two directions: agglomeration-aware schemes of the Mori–Tanaka or Eshelby type should be benchmarked against the two-stage scheme adopted here, and the coupling of the model with hydration and C-S-H models, in which the reacted fraction of nano-silica and the properties of the reaction products evolve with curing age, calibrated against nanoindentation and porosimetry data. Experimental campaigns on nano-SiO_2-reinforced concrete beams are also needed, both to validate the predicted frequencies and to calibrate the effective properties and the agglomeration parameters ξ and ζ against measured microstructural data (SEM, DLS) and beams of known mix proportions. Finally, the model could be extended to forced and damped vibration, nonlinear large-amplitude response, through-thickness functionally graded nanoparticle distributions, hybrid nanofiller systems (SiO_2 combined with CNTs or graphene) and plate and shell configurations, and it could account for the long-term aging and environmental effects on the agglomeration state and the dynamic performance.

Author Contributions: Conceptualization, H.R.S., Z.R.H., M.C. and E.H.; methodology, H.R.S., Z.R.H. and M.I.A.B.; software, M.C. and E.H.; validation, H.R.S., Z.R.H., M.I.A.B. and E.H.; formal analysis, H.R.S., Z.R.H., M.I.A.B. and M.C.; investigation, H.R.S., Z.R.H. and M.I.A.B.; resources, M.I.A.B. and M.C.; writing—original draft preparation, H.R.S., Z.R.H. and M.C.; writing—review and editing, M.I.A.B. and E.H.; visualization, H.R.S., Z.R.H. and E.H.; supervision, M.I.A.B. and M.C.; project administration, E.H. All authors have read and agreed to the published version of the manuscript.

Funding: This research received no external funding.

Institutional Review Board Statement: Not applicable.

Informed Consent Statement: Not applicable.

Data Availability Statement: The data presented in this study are fully within the article.

Conflicts of Interest: The authors declare no conflicts of interest.

References

1. Mohammed, T.U.; Rony, M.A.; Zunaied Bin Harun, M.; Uddin, N.; Saha, D.; Rahman, M.N.; Mahmood, A.H. Alternative Fine Aggregates to Natural River Sand for Manufactured Concrete Ensuring Circular Economy. *Constr. Mater.* **2024**, *4*, 640–654. https://doi.org/10.3390/constrmater4040035.
2. Zubarev, K.P.; Razveeva, I.; Beskopylny, A.N.; Stel'makh, S.A.; Shcherban', E.M.; Mailyan, L.R.; Shakhalieva, D.M.; Chernil'nik, A.; Nikora, N.I. Predicting the Strength of Heavy Concrete Exposed to Aggressive Environmental Influences by Machine Learning Methods. *Buildings* **2025**, *15*, 3998. https://doi.org/10.3390/buildings15213998.
3. Shittu, R.A.; Alhamadi, F.; Sherief, M.; AlFantazi, A.; Alkaabi, A.K. Factors Influencing the Radiation Shielding Capacity of Concrete Exposed to Aggressive Arid Environment: A Comprehensive Review. *Int. J. Concr. Struct. Mater.* **2025**, *19*, 91. https://doi.org/10.1186/s40069-025-00817-w.
4. Sharma, N.; Seema; Paruthi, S. High Performance Geopolymer Concrete Incorporating Nano Silica: Experimental and Economic Assessment. *J. Struct. Integr. Maint.* **2025**, *10*, 4. https://doi.org/10.1080/24705314.2025.2581357.
5. Mydin, M.A.O.; Tobbala, D.E.; Omar, R.; Muthusamy, K.; Thomas, B.S.; Abdullah, M.M.A.B.; Awoyera, P.O.; Fadugba, O.G.; Sor, N.H. Improving the Elevated Temperature Behaviour of Foamed Concrete through Nano Titania Addition and Microstructure Control. *Sci. Rep.* **2026**, *16*, 23282. https://doi.org/10.1038/s41598-026-54484-2.
6. Sharma, N.; Seema; Paruthi, S.; Khan, A.H.; Almalki, A.; Zeyad, A.M.; El-Abbasy, A.A. Advancing GGBS Geopolymer Concrete with Nano-Alumina: A Study on Strength and Durability in Aggressive Environments. *Rev. Adv. Mater. Sci.* **2025**, *64*, 20250142. https://doi.org/10.1515/rams-2025-0142.

7. Chen, Q.; Shi, X.; Gao, H.; Ma, J.; Chen, B. Mechanism of Nano-$CaCO_3$ in Modifying the Pore Structure of Foam Concrete: Characterization Based on X-CT and Theoretical Water Absorption Model. *Constr. Build. Mater.* **2026**, *540*, 147640. https://doi.org/10.1016/j.conbuildmat.2026.147640.
8. Hong, S.-H.; Choi, J.-S.; Lee, H.-J.; Yoon, Y.-S. Thermal and Sound Insulation Characteristics of CNT Infused Ultra-High-Strength Lightweight Concrete (UHSLC). *Cem. Concr. Compos.* **2025**, *164*, 106221. https://doi.org/10.1016/j.cemconcomp.2025.106221.
9. Abhilash, P.P.; Nayak, D.K.; Sangoju, B.; Kumar, R.; Kumar, V. Effect of Nano-Silica in Concrete: A Review. *Constr. Build. Mater.* **2021**, *278*, 122347. https://doi.org/10.1016/j.conbuildmat.2021.122347.
10. Chen, W.; Chen, X.-F.; Liang, R.; Sun, G. Synergistic Enhancement of Microstructure–Property Relationship in High-Volume Industry Waste Cementitious Composites via Graphene Oxide/Silica Fume Hybridization. *Constr. Build. Mater.* **2025**, *490*, 142520. https://doi.org/10.1016/j.conbuildmat.2025.142520.
11. Hamed, N.; Ismail, M.K.; Serag, M.I.; El-Attar, M.; El-Feky, M.S. The Role of Nano-Silica and Cellulose Nanofibers in Enhancing High-Early-Strength Concrete. *J. Sustain. Cem.-Based Mater.* **2026**, *15*, 2316–2346. https://doi.org/10.1080/21650373.2026.2643783.
12. Chen, Y.X.; Li, S.; Mezari, B.; Hensen, E.J.M.; Yu, R.; Schollbach, K.; Brouwers, H.J.H.; Yu, Q. Effect of Highly Dispersed Colloidal Olivine Nano-Silica on Early Age Properties of Ultra-High Performance Concrete. *Cem. Concr. Compos.* **2022**, *131*, 104564. https://doi.org/10.1016/j.cemconcomp.2022.104564.
13. Verma, P.; Shukla, S.; Pal, P. A Comprehensive Review on Dispersion Techniques of Nano-SiO_2 in Concrete Matrix. *Innov. Infrastruct. Solut.* **2025**, *10*, 304. https://doi.org/10.1007/s41062-025-02098-4.
14. Yang, T.; Liu, B.; Li, L.; Gan, X.; Lu, L.; Li, Y. Agglomeration Behavior of Colloidal Nano-Silica and Its Effect on Pore Structure, Mechanical Properties and Shrinkage of Cement Mortar. *Constr. Build. Mater.* **2023**, *409*, 133865. https://doi.org/10.1016/j.conbuildmat.2023.133865.
15. Liu, H.; Feng, C.; Fan, Y.; Hang, Z.; Zhang, J. A Unified Hybrid Micromechanical Model for Predicting the Thermal and Electrical Conductivity of Graphene Reinforced Porous and Saturated Cement Composites. *Compos. Struct.* **2024**, *340*, 118202. https://doi.org/10.1016/j.compstruct.2024.118202.
16. Voigt, W. Ueber die Beziehung zwischen den beiden Elasticitätsconstanten isotroper Körper. *Ann. Phys.* **1889**, *274*, 573–587. https://doi.org/10.1002/andp.18892741206.
17. Reuss, A. Berechnung der Fließgrenze von Mischkristallen auf Grund der Plastizitätsbedingung für Einkristalle. *Z. Angew. Math. Mech.* **1929**, *9*, 49–58. https://doi.org/10.1002/zamm.19290090104.
18. Hashin, Z.; Shtrikman, S. A Variational Approach to the Theory of the Elastic Behaviour of Multiphase Materials. *J. Mech. Phys. Solids* **1963**, *11*, 127–140. https://doi.org/10.1016/0022-5096(63)90060-7.
19. Eshelby, J.D. The Determination of the Elastic Field of an Ellipsoidal Inclusion, and Related Problems. *Proc. R. Soc. A* **1957**, *241*, 376–396. https://doi.org/10.1098/rspa.1957.0133.
20. Mori, T.; Tanaka, K. Average Stress in Matrix and Average Elastic Energy of Materials with Misfitting Inclusions. *Acta Metall.* **1973**, *21*, 571–574. https://doi.org/10.1016/0001-6160(73)90064-3.
21. Benveniste, Y. A New Approach to the Application of Mori-Tanaka's Theory in Composite Materials. *Mech. Mater.* **1987**, *6*, 147–157. https://doi.org/10.1016/0167-6636(87)90005-6.
22. Kontou, E. Studying the Effect of Agglomerates on the Mechanical Enhancement of Polymer Nanocomposites Using a Semiempirical Model. *Nanomaterials* **2026**, *16*, 477. https://doi.org/10.3390/nano16080477.
23. Pan, J.; Bian, L. Influence of Agglomeration Parameters on Carbon Nanotube Composites. *Acta Mech.* **2017**, *228*, 2207–2217. https://doi.org/10.1007/s00707-017-1820-9.
24. Maurya, M.C.; Jawaid, S.M.A.; Chakrabarti, A. Response of Agglomerated SWCNT Reinforced Nanocomposite Plate under Hygro-Thermal Loading. *Mech. Adv. Compos. Struct.* **2024**, *11*, 11–40. https://doi.org/10.22075/macs.2023.29697.1472.
25. Demir, E.C.; Benkaddour, A.; Aldrich, D.R.; McDermott, M.T.; Kim, C.I.; Ayranci, C. A Predictive Model towards Understanding the Effect of Reinforcement Agglomeration on the Stiffness of Nanocomposites. *J. Compos. Mater.* **2022**, *56*, 1591–1604. https://doi.org/10.1177/00219983221076639.
26. Javed, S. Mechanical Vibration Response of CNT-Reinforced Nanocomposite Conical Shells Using the Mori–Tanaka Micromechanics Model and FSDT. *AIMS Math.* **2025**, *10*, 29552–29581. https://doi.org/10.3934/math.20251298.
27. Timoshenko, S.P. LXVI. On the Correction for Shear of the Differential Equation for Transverse Vibrations of Prismatic Bars. *Lond. Edinb. Dubl. Philos. Mag. J. Sci.* **1921**, *41*, 744–746. https://doi.org/10.1080/14786442108636264.
28. Boukhelf, F.; Bouiadjra, M.B.; Bouremana, M.; Tounsi, A. Hygro-Thermo-Mechanical Bending Analysis of FGM Plates Using a New HSDT. *Smart Struct. Syst.* **2018**, *21*, 75–97. https://doi.org/10.12989/sss.2018.21.1.075.

29. Reddy, J.N. A Simple Higher-Order Theory for Laminated Composite Plates. *J. Appl. Mech.* **1984**, *51*, 745–752. https://doi.org/10.1115/1.3167719.
30. Touratier, M. A Generalization of Shear Deformation Theories for Axisymmetric Multilayered Shells. *Int. J. Solids Struct.* **1992**, *29*, 1379–1399. https://doi.org/10.1016/0020-7683(92)90085-8.
31. Soldatos, K.P. A Transverse Shear Deformation Theory for Homogeneous Monoclinic Plates. *Acta Mech.* **1992**, *94*, 195–220. https://doi.org/10.1007/BF01176650.
32. Karama, M.; Afaq, K.S.; Mistou, S. A New Theory for Laminated Composite Plates. *Proc. Inst. Mech. Eng. Part L J. Mater. Des. Appl.* **2009**, *223*, 53–62. https://doi.org/10.1243/14644207JMDA189.
33. Zamanian, M.; Kolahchi, R.; Bidgoli, M.R. Agglomeration Effects on the Buckling Behaviour of Embedded Concrete Columns Reinforced with SiO_2 Nano-Particles. *Wind Struct.* **2017**, *24*, 43–57. https://doi.org/10.12989/was.2017.24.1.043.
34. Shokravi, M. Buckling Control of Concrete Beams Reinforced with Smart Nanoparticles Using Numerical Methods. *Eur. J. Environ. Civ. Eng.* **2021**, *25*, 1349–1363. https://doi.org/10.1080/19648189.2019.1578268.
35. Arani, A.J.; Kolahchi, R. Buckling Analysis of Embedded Concrete Columns Armed with Carbon Nanotubes. *Comput. Concr.* **2016**, *17*, 567–578. https://doi.org/10.12989/cac.2016.17.5.567.
36. Dine Elhennani, S.; Harrat, Z.R.; Chatbi, M.; Belbachir, A.; Krour, B.; Işık, E.; Harirchian, E.; Bouremana, M.; Bachir Bouiadjra, M. Buckling and Free Vibration Analyses of Various Nanoparticle Reinforced Concrete Beams Resting on Multi-Parameter Elastic Foundations. *Materials* **2023**, *16*, 5865. https://doi.org/10.3390/ma16175865.
37. Winkler, E. *Die Lehre von Elastizitat und Festigkeit (on Elasticity and Fixity)*; Dominicus: Prague, Czech Republic, 1867.
38. Filonenko-Borodich, M.M. Some Approximate Theories of the Elastic Foundation. *Uch. Zap. Mosk. Gos. Univ. Mekh.* **1940**, *46*, 3–18.
39. Hetényi, M. *Beams on Elastic Foundations*; University of Michigan Press: Ann Arbor, MI, USA, 1946.
40. Pronk, A. The Pasternak Foundation: An Attractive Alternative for the Winkler Foundation. In Proceedings of the ICCP, West Lafayette, IN, USA, 20–22 April 1993.
41. Kerr, A.D. Elastic and Viscoelastic Foundation Models. *J. Appl. Mech.* **1964**, *31*, 491–498. https://doi.org/10.1115/1.3629667.
42. Dutta, S.C.; Roy, R. A Critical Review on Idealization and Modeling for Interaction among Soil–Foundation–Structure System. *Comput. Struct.* **2002**, *80*, 1579–1594. https://doi.org/10.1016/S0045-7949(02)00115-3.
43. Harrat, Z.R.; Chatbi, M.; Krour, B.; Amziane, S.; Bouiadjra, M.B.; Hadzima-Nyarko, M.; Radu, D.; Işik, E. Bending Analysis of Nano-Fe_2O_3 Reinforced Concrete Slabs Exposed to Temperature Fields and Supported by Viscoelastic Foundation. *Adv. Concr. Constr.* **2024**, *17*, 111–126. https://doi.org/10.12989/acc.2024.17.2.111.
44. Damrongwiriyanupap, N.; Detphan, C.; Chompoovong, K.; Phoo-ngernkham, T.; Hanjitsuwan, S.; Sae-Long, W.; Petcherdchoo, A.; Sukontasukkul, P.; Chindaprasirt, P. Sustainable and Cost-Effective Repair Material: The Role of Reactive SiO_2 in Alkali-Activated Binders. *J. King Saud Univ. Eng. Sci.* **2025**, *37*, 10. https://doi.org/10.1007/s44444-025-00015-9.
45. Raveendran, N.; Vasugi, K. Synergistic Effect of Nano Silica and Metakaolin on Mechanical and Microstructural Properties of Concrete: An Approach of Response Surface Methodology. *Case Stud. Constr. Mater.* **2024**, *20*, e03196. https://doi.org/10.1016/j.cscm.2024.e03196.
46. Amran, M.; Al-Fakih, A.; Chu, S.H.; Fediuk, R.; Haruna, S.; Azevedo, A.; Vatin, N. Long-Term Durability Properties of Geopolymer Concrete: An In-Depth Review. *Case Stud. Constr. Mater.* **2021**, *15*, e00661. https://doi.org/10.1016/j.cscm.2021.e00661.
47. Deb, P.S.; Sarker, P.K.; Barbhuiya, S. Effects of Nano-Silica on the Strength Development of Geopolymer Cured at Room Temperature. *Constr. Build. Mater.* **2015**, *101*, 675–683. https://doi.org/10.1016/j.conbuildmat.2015.10.044.
48. Wang, M.; Liu, S.; Zhang, C.; Wu, Y.; Wang, L.; Guo, T. Performance Evolution and Microstructure Optimization of Recycled Fine Aggregate Rapid-Hardening Sulfoaluminate Cement Mortar by Nano-SiO_2 Surface Modification. *Nanomaterials* **2026**, *16*, 1051. https://doi.org/10.3390/nano16171051.
49. Malaiškienė, J.; Škamat, J.; Kizinievič, O.; Girskas, G. Synergistic Effect of Metakaolin Waste and Nano-Silica on the Properties of Ultra-High-Performance Concrete. *Processes* **2025**, *13*, 3614. https://doi.org/10.3390/pr13113614.
50. Carneiro, L.R.S.; Houmard, M.; Rocha, V.V.; Ludvig, P. The Effect of Nanosilica Incorporation on the Properties of Cement-Based Materials with and Without Other Supplementary Admixtures—A Literature Review. *Open Constr. Build. Technol. J.* **2022**, *16*, e2207290. https://doi.org/10.2174/18748368-v16-e2207290.
51. Hendrix, D.; Wille, K. Stabilizing Dispersed Colloidal Nanosilica Exposed to an Ultra-High Performance Concrete Environment. *Constr. Build. Mater.* **2023**, *409*, 133975. https://doi.org/10.1016/j.conbuildmat.2023.133975.

52. Kong, D.; Du, X.; Wei, S.; Zhang, H.; Yang, Y.; Shah, S.P. Influence of Nano-Silica Agglomeration on Microstructure and Properties of the Hardened Cement-Based Materials. *Constr. Build. Mater.* **2012**, *37*, 707–715. https://doi.org/10.1016/j.conbuildmat.2012.08.006.
53. Serag, M.I.; El-Kady, H.; El-Feky, M.S. The Effect of Indirect Sonication on the Reactivity of Nano Silica Concrete. *Int. J. Sci. Eng. Res.* **2014**, *5*, 334.
54. Benbakhti, A.; Benfrid, A.; Chatbi, M.; Harrat, Z.R.; Bachir Bouiadjra, M. Validation of the Reuss–Voigt Homogenisation Model for Glass Powder-Based Eco-Concretes. *Eurasia Proc. Sci. Technol. Eng. Math.* **2023**, *26*, 93–99. https://doi.org/10.55549/epstem.1409404.
55. Harrat, Z.R.; Amziane, S.; Krour, B.; Bouiadjra, M.B. On the Static Behavior of Nano SiO_2-Based Concrete Beams Resting on an Elastic Foundation. *Comput. Concr.* **2021**, *27*, 575–583. https://doi.org/10.12989/cac.2021.27.6.575.
56. Paul, B. Prediction of Elastic Constants of Multiphase Materials. Trans. Metall. Soc. *AIME* **1960**, *218*, 36–41.
57. Sobhy, M. Buckling and Free Vibration of Exponentially Graded Sandwich Plates Resting on Elastic Foundations under Various Boundary Conditions. *Compos. Struct*. **2013**, *99*, 76–87. https://doi.org/10.1016/j.compstruct.2012.11.018.
58. Jia, S.; Yang, G.; Pu, Y.; Ma, P.; Li, K. Free Vibration Characteristics of Functionally Graded Material (FGM) Beams on Three-Parameter Viscoelastic Foundation. *J. Compos. Sci.* **2025**, *9*, 215. https://doi.org/10.3390/jcs9050215.
59. Şimşek, M. Fundamental Frequency Analysis of Functionally Graded Beams by Using Different Higher-Order Beam Theories. *Nucl. Eng. Des.* **2010**, *240*, 697–705. https://doi.org/10.1016/j.nucengdes.2009.12.013.

Disclaimer/Publisher's Note: The statements, opinions and data contained in all publications are solely those of the individual author(s) and contributor(s) and not of MDPI and/or the editor(s). MDPI and/or the editor(s) disclaim responsibility for any injury to people or property resulting from any ideas, methods, instructions or products referred to in the content.